Experimental-Numerical Analysis of Gasoline Spray-Wall Impingement at Ultra-High Injection Pressure for GCI Application

Experimental-Numerical Analysis of Gasoline Spray-wall Impingement at Ultra-high Injection Pressure for GCI Application.

Davide Viscione*, Valerio Mariani*, Gian Marco Bianchi, Stefania Falfari, Vittorio Ravaglioli, Giacomo Silvagni

Department Of Industrial Engineering (DIN), University of Bologna, Alma Mater Studiorum, Italy

Alessandro Montanaro, Luigi Allocca

STEMS – CNR, Napoli, Italy

*Correspondence: Davide Viscione, davide.viscione2@unibo.it; Valerio Mariani, valerio.mariani4@unibo.it

Abstract

Nowadays, in the perspective of a full electric automotive scenario, internal combustion engines can still play a central role in the fulfilment of different needs if the efficiency will be improved, and the tailpipe emission will be further limited. Gasoline Compression Ignition engines can offer a favourable balance between NOx, particulate, operating range. Stable operations are ensured by ultra-high gasoline injection pressure and tailored injection patterns in order to design the most proper local fuel distribution. In this context, engine simulations by means of CFD codes can provide insights on the design of the injection parameters, and emphasis must be placed on the capture of spray-wall impingement behaviour under those non-conventional conditions. This paper aims to analyse the spray-wall impingement behaviour of ultra-high gasoline spray using a combined experimental-CFD approach. The fuel is injected inside a vessel through a single-hole nozzle at GCI-like injection pressure (500-700 bar) against a metal surface. At the test bench, optical measures were performed by means of the Mie-scattering technique in order to capture the impact morphology. Furthermore, some synthetic features of the impact were calculated, namely the thickness and the width of the rebound cloud. In order to focus on the wall film formation mechanism, the tests were conducted at room temperature. Then, the experimental data were used to validate the CFD spray-wall impingement methodology and tuning.

Keywords

- Ultra-high gasoline injection pressure
- CFD spray wall impingement
- Mie Scattering spray wall impingement

Introduction

Continuous stringent regulations on the pollutants released by an internal combustion engine have pushed the automotive industries towards innovative solutions. With the increased adoption of electrified powertrains, the optimization of the internal combustion engine is one of the short-midterm solutions to overcome the limitations imposed by the new homologation standards. Several studies state that the adoption of Low-Temperature Combustion (LTC) systems has the potential to simultaneously increase the engine efficiency while reducing the pollutant emissions [1]. Among the different systems, Gasoline Compression Ignition (GCI) engines are recognized as one of the most promising solutions due to their capability to cover a wide range of the engine operative map with a simple control of the combustion phasing [2]. Indeed, the GCI engine is operated with multiple-late injections performed around the top-dead centre in the compression stroke to stratify the charge, leading to the generation of mixing-controlled diffusion combustions to deliver the requested torque [3].

Since the GCI combustion is strongly dependent on the local mixture conditions, in the view of optimizing such concept, three-dimensional Computational Fluid Dynamics (CFD) simulations are effective tools to investigate the three-dimensional local effects of the injection features. Considering the typical injection pattern adopted in GCI applications, the spray dynamics and the interaction between the liquid spray and the engine walls are key points for both the local mixture and pollutant emissions generation.

In this context, putting effort in the setting of a methodology able to reproduce the fuel wall film formation and particle rebound after the wall impingement is mandatory for a robust prediction of the local mixture composition. Many authors reported similar works for gasoline direct injection [4–6] and Common Rail (CR) [7,8] injectors for gasoline and Diesel sprays, respectively. Considering that the experimental tests on the GCI engine [9,10] have been made converting a conventional Diesel engine to simply elaborate gasoline in its CR system, the conditions at which the fuel is operated have been scarcely investigated. This paper presents a preliminary investigation of the fuel behaviour at impinging conditions against a surface at ambient temperature. Firstly, the experimental and computational methods are presented. Then, a comparison between experimental and numerical results is made in terms of thickness and width of the rebounded fuel clouds.

Experimental setup

In this section, the setup and methodology for the impact study of the fuel on a flat wall, coupled with its split in spread and rebound mode in a quiescent ambient filled with gas at atmospheric backpressure, will be described. Non-intrusive Mie-scattering technique was used in a vessel through wide quartz optical accesses for the visualization of the shot. Commercial gasoline at constant temperature of 25 °C was injected by an adapted CR Diesel system. The fuel comes from a single-hole axially disposed injector (characteristics in Table 1), and impacts on an aluminum plate (1.077 µm average roughness measured by the Stylus Profilometer), 80 mm in diameter and perpendicularly positioned at 30.0 mm from the nozzle tip. For this work, a wall temperature (T_w) of 25 °C was fixed. More details on the impact setup were reported in [11].

Table 1: Injector geometric characteristics.

Number of nozzles	1
Hole diameter	100 µm
Length of the nozzle	1000 µm
Conicity	0

The behavior of the liquid, spreading after the impact, was studied applying the optical technique enlightening the liquid by a high-power flash lamp synchronized with the injection. The Mie-scattering section, branch of the more general Mie-schlieren technique and reported in [12], was adopted. The images of the evolving impact were acquired in a cycle-resolved mode by a Photron Fastcam SA4 high-speed camera with time-resolution 92.6 ms, the calibration factor was set at 12.1 pixel/mm. Five consecutive iterations were carried out to obtain an evaluation of the jet spreads on the measurements. Thus, the measurements were averaged on five consecutive injections to take into account the cycle-to-cycle variability giving up an analysis of the spread. The experimental results, reported in the Results section, represent the average of the five measurements for each instant for both the width and the thickness. The corresponding error bars, reported per each time, indicate the standard deviation respect to the mean value.

The impact phenomenon was characterized by two synthetic measurements on the rebounded spray cloud, the tangential penetration (width) and the axial penetration (thickness). A customized image process was carried out for the objective identification of the width, as the farther distance respect to the spray axis, and the thickness, as the highest presence of the fuel respect to the wall surface. Due to the axial-symmetry of the phenomenon, half impact was processed for resource saving. The Mie-scattering pictures were treated through a customized algorithm developed in C#. Net ambient to better outline the contours of the liquid.

The extract contour of the rebound shapes allows us to obtain, through the set calibration, the evolution of the width and thickness parameters. Figure 1 shows a sequence of the images along the processing procedure of the fuel impact. Once identified the image and the parameters of interest, an automated procedure was applied on all the image sequences to determine the mean values and standard errors for the widths and thicknesses. Background subtraction, gamma correction, morphology filtering, levels linear, gaussian blur and threshold filtering as well as the fill hole operation were applied on the Mie-scattering images to enhance the jet figures. Finally, a contour detection allowed to identify their boundaries. A batch method extracted the width and thickness as a function of the ambient pressure and wall temperature. Further details of the image processing applied to the spray impact are reported in [13,14].

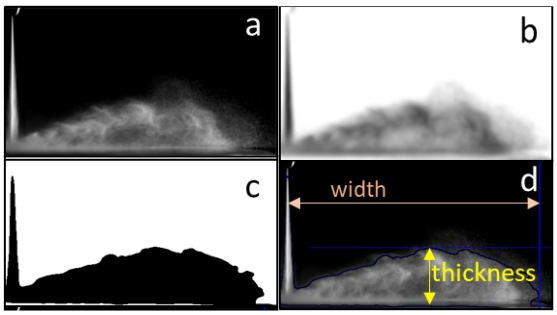

Figure 1: Example of image processing algorithm applied to the impact: a) raw image; b) processed image; c) binarized image for contour extraction; d) outlines with width and thickness defined through the technique.

In order to provide numerical simulations with the injection flow rate profile, the single-hole injector was characterized in terms of instantaneous injected mass. The dynamic characterization was conducted with an AVL Injection Rate Meter according to the "Bosch pipeline" principle [15]. A GMD12D – AVL piezoquartz transducer measures the pressure increase in the cockpit (Δpg), which is then transformed in fuel rate (q [mm^3/s]) according to Eq. (1) through the chemical-physical properties of the fluid (ρ is the fuel density, a the speed sound in the fluid) and the cross section of the tube pipe (A). The time resolution of the fuel rate is set at 5 μs. The final flow rate profiles can be seen in Figure 2.

$$q(t) = \frac{\Delta p_g \, A}{\rho \, a} \cdot 10^5 \qquad (1)$$

To impose the flow rate curves in the CFD simulations, the traces of Figure 2 have been filtered to eliminate the spikes provided by the experiments.

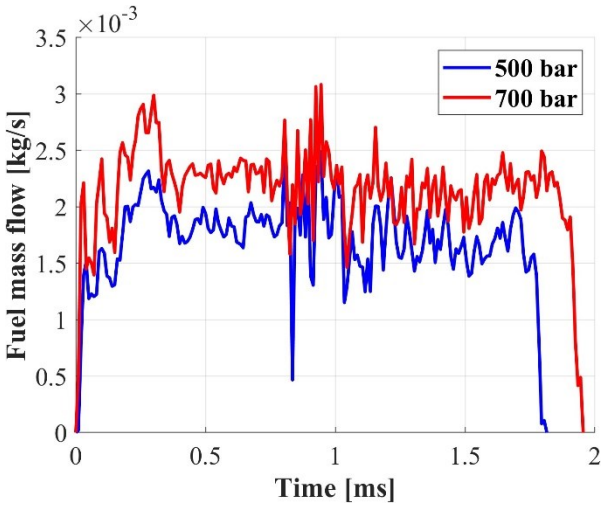

Figure 2: Mass flow rate curves for injection pressures of 500 and 700 bar.

3D-CFD Simulations

In this section, the methodology for three-dimensional CFD simulations is presented. Firstly, the main characteristics of the computational mesh are highlighted. Then, the models used to simulate the liquid spray are explained.

Mesh generation

The commercial software STAR-CD 4.28 by Siemens is used to simulate the fuel impinging dynamics. The computational domain was modelled as a squared section box of sizes 80 x 80 x 40 mm. All the box faces are set as walls with fixed temperature (25 °C). The dimensions of the box have been determined in order to prevent the interaction between the spray cloud and the vertical walls. A minimum cell size of 0.25 mm has been chosen to allow the hypothesis of dispersed phase of the liquid droplets treated with the Lagrangian approach. In particular, the minimum mesh size was obtained by refining the base size (4 mm) four times around the injector location in order to properly capture the primary break-up process. From the injector tip zone, the mesh coarsens up to 0.5 mm for a distance of 10 mm from the injection point. Furthermore, a mesh refinement of size 1 mm was adopted based on the propagation of the rebound cloud provided by experiments. Figure 3 highlights the mesh geometry in section view and the refinements described above.

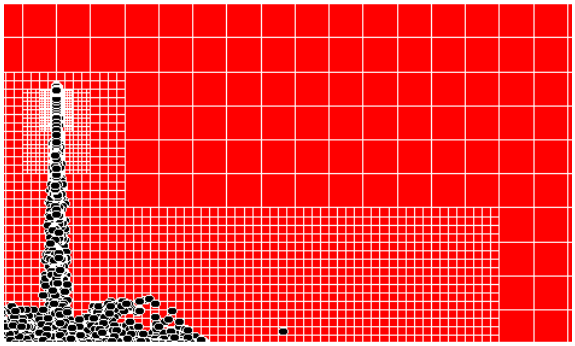

Figure 3: Visualization of the grid geometry in section view. Cell size: 4 mm base, 1mm in the L-shaped zone, 0.5 mm in the coarser tip-zone, 0.25 mm in the finer tip-zone.

Regarding both the fuel vapor and liquid phases, a pseudo-pure fluid representing the commercial Research Octane Number (RON) 95 gasoline was selected from the STAR-CD built-in NIST database. The main properties of the pseudo-pure liquid are listed in Table 2.

Table 2: NIST properties of the pseudo-pure liquid chosen to represent commercial gasoline.

Molecular weight	102 g/mol
Critical temperature	544 K
Critical pressure	25.7 bar
Density @30 °C	744.020 kg/m^3
Viscosity @30 °C	0.448 mPa s
Surface tension @30 °C	0.224 N/m
Specific heat @30 °C	1.861 kJ/kg/K
Latent heat @30°C	337.810 kJ/kg
Saturation pressure @30 °C	0.077 bar

The Reynolds Averaged Navier-Stokes (RANS) approach have been adopted, with the k − ϵ RNG model to capture turbulence. The Pressure Implicit with Splitting Operators (PISO) has been selected as the solution algorithm. Momentum, turbulence, temperature, and density have been discretized by the second order central difference method. A fixed time step of 1 μs is set.

Lagrangian models

For the present work, the droplet initialization follows a user sub-routine [16] based on a modified version of the Huh & Gosman atomization model [17]. In particular, the user-subroutine takes into consideration the transient fluid dynamics during the early-opening stages of the injection event by modifying both the droplet initial diameter and the spray cone angle. Instead, during the steady state phase, the effective diameter of the droplets is calculated starting from the evaluation of the discharge coefficient (C_d), as Eq. (2) states:

$$C_d = \frac{\dot{m}}{\dot{m}_{th}} = \frac{\dot{m}}{A_g\sqrt{2\rho_{fuel}\Delta p}} \quad (2)$$

where $\dot{m}$ is the fuel mass flow rate at steady state, A_g is the geometrical area of the nozzle, ρ_{fuel} the fuel density, and Δp the pressure-drop facing the injector. The discharge coefficient considers both the reduction of the velocity given by friction (C_v) and the reduction of the flowing area due to the vena contract phenomenon (C_c), as Eq. (3) states.

$$C_d = C_v C_c \quad (3)$$

Starting from an estimation of the C_v, the effective diameter D_{eff} is then computed from the nozzle geometric minimum internal diameter D_g as in Eq. (4):

$$D_{eff} = D_g\sqrt{C_c} \quad (4)$$

In order to take into account the transient dynamics during the injector opening stage, which results in different values of discharge coefficient [18,19] and cone angle, a user-subroutine has been implemented. In particular, the aim of the subroutine is to switch from the transient quantities to the ones calculated at steady state conditions considering the experimental data provided by the tests. Regarding the

'switch' time from transient dynamic-set values to steady state-set values at which the conversion must be done, Figure 4**Errore. L'origine riferimento non è stata trovata.** shows the contour plots of the experimental spray plumes at 500 bar (left) and 700 bar (right), highlighting the difference between the morphology in the early spray development (t = 93 µs) with respect to the one at the next sampling time (t = 186 µs). Considering that the light source comes from the right side, it is possible to notice that the cone angle during the early stages is wider for the injection pressure of 500 bar. This evidence affects the impact angle with the wall as well, resulting in a different dynamic of the spray. For this reason, after calculations, the cone angle during the early spray development at 500 bar has been imposed at 6 degrees, with the one at steady state calculated to be almost 4 degrees. Instead, for the condition at 700 bar, the cone angle is almost fixed at the same value of 4 degrees for the whole experiment time. Moreover, also the diameter of the introduced droplets in the same time range is different from the one at steady state.

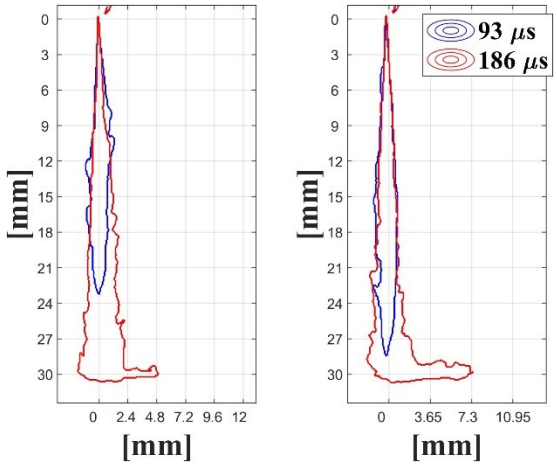

Figure 4: contour plots of the experimental spray plumes at two consecutive times at the injection pressure of 500 bar(left) and 700 bar (right).

In fact, if the diameter is the same as the one during the steady state phase, a much more reduced Liquid Length Penetration (LLP) is induced, as shown in the lowest points of Figure 5,**Errore. L'origine riferimento non è stata trovata.** an effective diameter of almost 72 µm allows to match the experimental LLP at t = 93 µs for an injection pressure of 500 bar, and 70 µm for 700 bar. Instead, while the fuel mass flow approaches the steady-state phase, the diameter of the introduced droplets switches to the steady-state value.

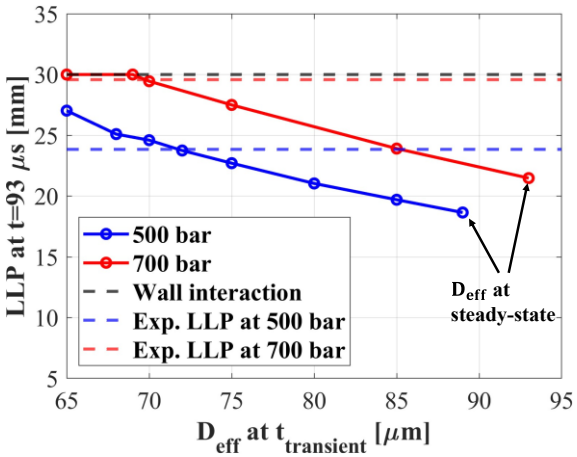

Figure 5: LLP in function of the effective diameter during the transient stage.

Once droplets are introduced, their breakup due to the aerodynamic drag is modelled with the Pilch-Erdman approach [20]. For this model, break-up occurs if the droplet Weber number (Eq. (5)) overcomes a critical threshold (Eq. (6)) ($We > We_c$):

$$We = \frac{\rho_d |\boldsymbol{u} - \boldsymbol{u_d}|^2 D_d}{\sigma_d} \quad (5)$$

$$We_c = 12(1 + 1.077(Oh)^{1.6}) \quad (6)$$

Where ρ_d represents the fuel density, D_d the droplet diameter, σ_d the fuel surface tension, $u - u_d$ the relative velocity between air and fuel droplets, and $Oh = \frac{\mu_d}{(\rho_d D_d \sigma_d)^{0.5}}$ is the Ohnesorge number (μ_d is the fuel dynamic viscosity).

According to the actual value of We, five dimensionless total break-up times T are given in Table 3.

Table 3: Dimensionless total break-up times T according to Pilch and Erdmann.

Break-up regime	Dimensionless total break-up times T	Range of We
Vibrational	$T = 6(We - 12)^{-0.25}$	$12 < We < 18$
Bag	$T = 2.45(We - 12)^{0.25}$	$18 < We < 45$
Bag-and-stamen	$T = 14.1(We - 12)^{-0.25}$	$45 < We < 350$
Sheet stripping	$T = 0.766(We - 12)^{0.25}$	$350 < We < 2670$
Wave crest stripping	5.5	$2670 < We$

Then, the total break-up time is calculated as in Eq. (7):

$$\tau = T \frac{D_d}{|u - u_d|} \left(\frac{\rho_d}{\rho}\right)^{0.5} \quad (7)$$

Once the break-up event occurs, the droplet diameter changes according to Eq. (8):

$$\frac{dD_d}{dt} = -\frac{D_d - D_s}{\tau} \quad (8)$$

With the D_s the stable diameter, which is obtained from Eq. (9):

$$D_s = We_c \frac{\sigma_d}{\rho|\boldsymbol{u} - \boldsymbol{u_d}|^2}\left(1 - \frac{V_d}{|u - u_d|}\right)^{-2} \quad (9)$$

where $V_d = |\boldsymbol{u} - \boldsymbol{u_d}|\left(\frac{\rho}{\rho_d}\right)^{0.5}(0.375T + 0.2274T^2)$.

Once the liquid jet impacts with the walls, the interaction between the droplets and the wall is approached by means of the Bai-ONERA model, a STAR-CD built-in option based coupling the features of the Bai model [21], and the ONERA model [22] from the literature. The strong droplet temperature-dependence upon the wall is well known. In particular, for progressively higher wall temperatures from ambient conditions up to saturation conditions, the evaporation rate of a droplet increases. Then, starting from the so called Nukiyama temperature (T_N), the evaporation decelerates due to the insulating property of the nearly generated vapour phase. The further increase of the wall temperature leads to the minimum evaporation at the Leidenfrost temperature (T_L), for which a vapour film fully prevent the direct contact between droplets and the surface. For temperatures higher than T_L, the evaporation rate starts increasing again. The way those critical points affect the impact regimes can be described by a dimensionless temperature, which is defined as in Eq. (10) in the STAR-CD mixed implementation:

$$T^* = \frac{T_W - T_N}{T_L - T_N} \quad (10)$$

where T_W represents the wall temperature.

In STAR-CD, the Nukiyama temperature is defined by a multiplying factor of the fuel saturation temperature ($T_N = B_s T_{boiling}$). Considering that the literature provides a value of almost 440 K for the Nukiyama temperature of commercial gasolines ([8,23]), the B_s was set at 1.2 once a boiling temperature of 372 K was identified from the NIST database for gasoline at ambient pressure. The Leidenfrost temperature at ambient pressure (460 K) has been calculated by using the Spiegler correlation [24]. Since for the current study, the wall temperature has been set to the ambient one, $T^* < 0$.

From the kinetic point of view, in the Bai-ONERA model the fate of the droplet after the impingement is defined by the Sommerfeld number (Eq. (11)):

$$K = WeOh^{-0.4} = (We^2 Re)^{0.4} \quad (11)$$

where We is the Weber Number ($We = \frac{\rho_d v^2 D_d}{\sigma_d}$) and Re the Reynolds number ($Re = \frac{\rho_d v D_d}{\mu_d}$). In these equations, ρ represents the fuel density, v the droplet velocity magnitude along the surface perpendicular direction, D_d the droplet diameter, σ_d the fuel surface tension, and μ_d the fuel dynamic viscosity.

Consider the Bai-ONERA wall-impingement map in Figure 6. CFD simulation analyses reveal the droplet characteristics in correspondence of the impact region with the wall for an injection pressure of 500 bar. In particular, the diameter of the impinged droplets is around 32 µm, and the droplet velocity 230 m/s. Instead, for the greater injection pressure of 700 bar, the diameter of the impinged droplets is around 12 µm and the droplet velocity is 280 m/s. Considering the fuel density as 750 kg/m^3, the surface tension as 0.02 N/m and the dynamic viscosity as 0.0004 Pa · s, the logarithm of the resulting Sommerfeld number K is equal to 12.66 and 11.78 for the injection pressures of 500 and 700 bar, respectively.

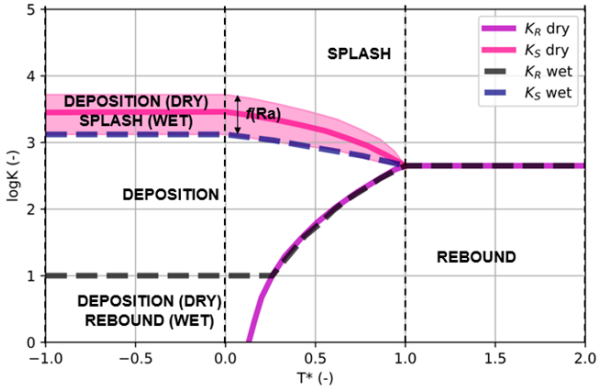

Figure 6: visualization of the impact regimes in function of K and wall temperature.

As a result, for those K values and $T^* < 0$, the impact events fall in the splash regime, in which each impinging droplet is split into two rebound droplets. From Figure 6 it is visible that at the present K values, the wall average roughness (Ra), which is responsible for the shift of the deposition-splash threshold, does not affect the fate of the injected droplets. In general, in the model it is assumed that the lower is the average surface roughness compared to the droplet diameter, the higher is the K_S threshold, i.e., the more likely is the deposition regime with respect to splash.

Moreover, in order to capture the overall experimental plume morphology, also the inter-droplet collision O'Rourke model [25] has been implemented. In fact, by only considering the momentum transfer between air and the droplets, the simulated spray behaviour shows a much more reduced overall diffusion from the impact region. Instead, by also considering the inter-droplet collision, the momentum exchange is provided also by coalescence, separation and bouncing between the droplets, enhancing the push of the rebound cloud towards the outer zones, leading to a better shape-match against experiments.

For the sake of clarity, Table 4 collects the main Eulerian-Lagrangian models ad set values adopted in this work.

Table 4: CFD simulation models setting.

Spray injection half-angle @500 bar/@700 bar	Transient 6 deg/4 deg Steady 4 deg/4 deg
Effective nozzle diam. @500 bar/@700 bar	Transient 75 µm/70 µm Steady 89 µm/70 µm

Breakup	Pilch and Erdmann [20]
Drag	Schillen and Naumann [26]
Evaporation	El Wakil [27]
Leidenfrost temp	Spiegler [24]
Wall interaction	Bai-ONERA [21,22]

Results

In this section, a comparative analysis of the fuel spray behaviour after the wall impingement is conducted by comparing the results obtained with the experiments and with the CFD simulations. In particular, the thickness and the width time evolution of the rebound cloud, and the overall impact morphology will be compared. Table 5 summarizes the test conditions that will be discussed.

Table 5: Test conditions.

Ambient pressure	1 bar
Ambient temperature	20°C
Injection pressure	500, 700 bar
Injected fuel	3.1 mg (500 bar), 4.2 mg (700 bar)
Energizing Time (ET)	1000 µs
Fuel temperature	25°C
Distance from wall	30 mm
Wall temperature	25°C

Calculation of the width and thickness of the plume

In this section, the computed width and thickness of the simulated and experimental plumes are compared. It is underlined that the injection event takes around 2 ms to be completed, however width and thickness measures are available up to a bit shorter time (around 1.5 ms). In particular, the latest experimental points are those at which the rebound cloud is fully included in to the camera window according to the installation distance.

Figure 7 shows the comparison between the experimental and simulated plume width at 500 (a) and 700 (b) bar, respectively. For the injection pressure of 500 bar, a slight overestimation of the plume width is evidenced, whilst in the late phase the simulated width is in good agreement with the experiments for both the injection pressure conditions. The width at 700 bar injection shows a nearly perfect match. The overestimation observed at the injection pressure of 500 bar can be attributed also to the sharp change of the discharge coefficient from the transient one to the steady one. In this condition, the discharge coefficient-associated quantities (e.g., flow rate, droplet initial diameter) change in an impulsive manner. As a result, the spray newly generated by the sharp change hits the wall with an instantaneous larger kinetic contribution. Thus, the associated rebounded cloud features a larger momentum resulting in a faster tangential penetration. Consequently, the width results to be slightly overestimated.

Concerning the thickness calculation, as shown in Figure 8(a), the simulated thickness at 500 bar is well correlated with the experiment and falls within the confidence bars for the whole time range. In the contrary, the simulated thickness for an injection pressure of 700 bar (Figure 8(b)) is under-estimated during the late phase of the event. In this condition the thickness of the simulated plume approaches a stable value (from 1500 µs at 500 bar, from 1000 µs at 700 bar), too. This could be due also to the definition of the threshold applied to the experimental images to estimate the thickness. In fact, with respect to the simulation, for which the droplets of the plume are well confined in a defined spatial region, the real liquid phase is more dispersed, as the next section will show. It must be also considered that in Lagrangian simulations, the dispersed phase is usually represented by the so called 'parcels', namely particles that are representative of a sample of droplets with the same characteristics (velocity, diameter, etc.). Thus, in CFD simulations is usual to process spray images that are less dense compared to the experimental ones.

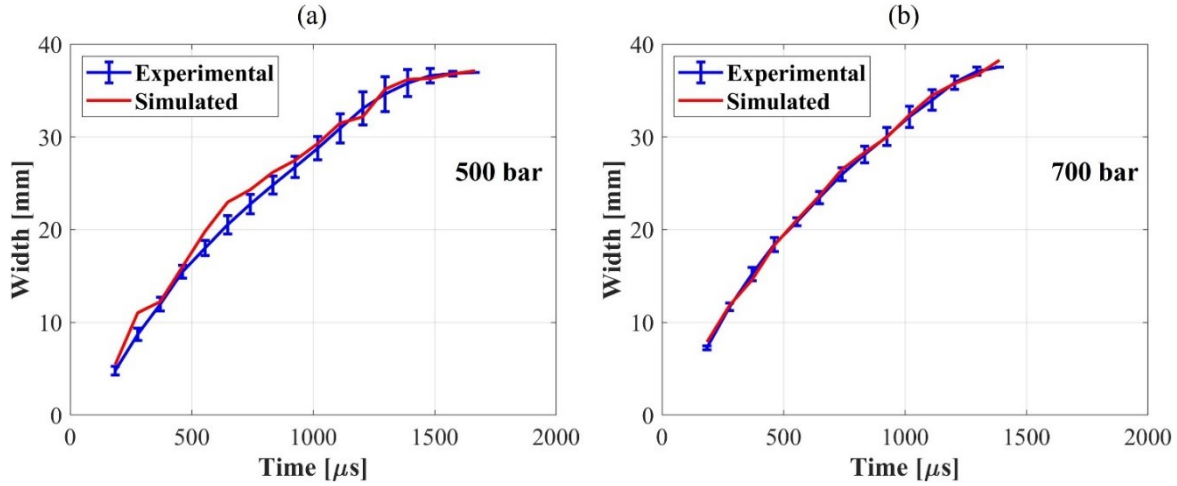

Figure 7: Comparison between the experimental and simulated spray at 500 bar(a) and 700 bar(b).

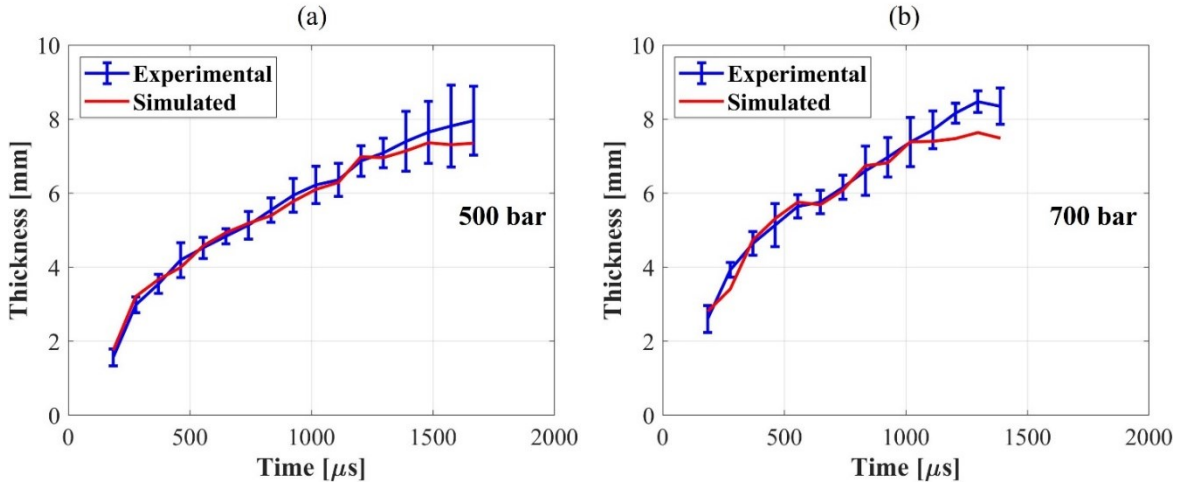

Figure 8: Comparison between the experimental and simulated spray thickness at 500 bar(a) and 700 bar(b).

In order to have a better comprehension of the simulated thickness underestimation, Figure 9 was crafted. Figure 9 shows the contour of both the experimental (top) and the simulated (bottom) spray plume contour at different instants (highlighted by different colours). The instants were chosen in order to compare the very early impact time (pink, 186 µs); a middle point of the thickness curves at which the experimental-numerical match is nice (blue, 740 µs); the first point at which the flattening of the simulated curve is observed (red, 1020 µs); the last point of the simulated flat behaviour (black, 1390 µs). Furthermore, for each instant it is reported the tangential coordinates range along which the maximum thickness can be identified.

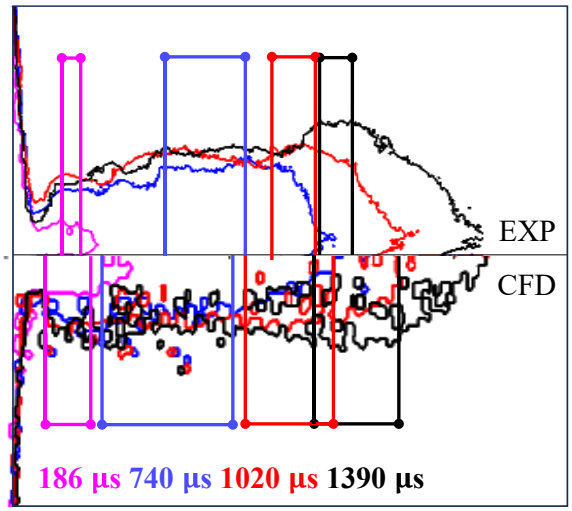

Figure 9: comparison of the contour plots of the simulated and experimental plumes for the injection pressure of 700 bar.

Considering the fully developed spray, it is visible that for the experimental image the more the time is shifted towards the latest phase of the injection, the narrower is the coordinate range of the maximum. This happens because of the enhancement of the upper rim shape of the cloud over time, which is promoted by the continuous blown produced by the impact. Focusing on the CFD image, it can be seen that the coordinate range of the maximum is still wider as well as less sensitive to the time. This is due to the fact that the CFD cloud evolves according to a flatter shape, thus, no clear blown-induced rim is captured. As a result, the maximum thickness approaches a nearly constant value.

Spray morphology

In this section, the comparison of the simulated and experimental impinged fuel spray plume morphology is made for a set of selected instants. These instants were chosen based on the curves in Figure 7 and Figure 8, considering that the graphical representation can contribute to understand how the simulation can be improved or where the adopted models allow to have good agreements with the real case.

As a first instant, the represented spray cloud for an injection pressure of 500 bar at t = 369 µs (Figure 10) highlights the over-estimation in the simulations. A slightly greater thickness can be noticed too, even if the deviation relies inside the experimental error bars of Figure 8(a).

On the other hand, the simulated spray plume shown in Figure 11 is able to capture both the thickness and width of the experimental one, as shown in Figure 7 and Figure 8. Moreover, the interaction between the droplets is effectively represented, since also the global shape of the rebounded cloud is almost the same with the one of the experiments.

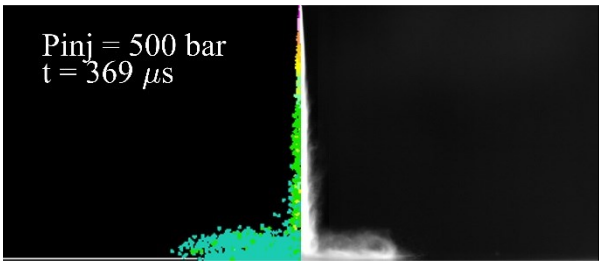

Figure 10: comparison of the experimental and simulated spray plume morphology for an injection pressure of 500 bar at t=369 μs.

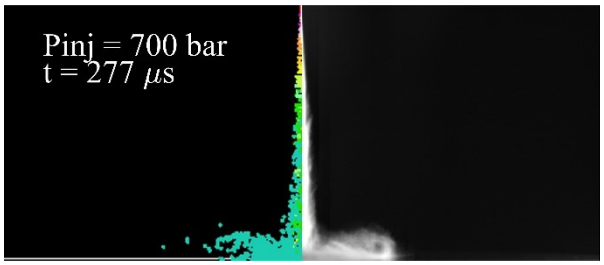

Figure 11: comparison of the experimental and simulated spray plume morphology for an injection pressure of 700 bar at t=277 μs.

The next figures refer to the comparison between the simulated and experimental spray plumes during the late injection events, the aim is to understand the similarities and deviations highlighted in Figure 7 and Figure 8.

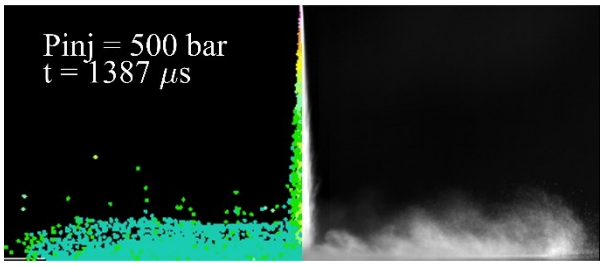

Figure 12: comparison of the experimental and simulated spray plume morphology for an injection pressure of 500 bar at t=1387 μs.

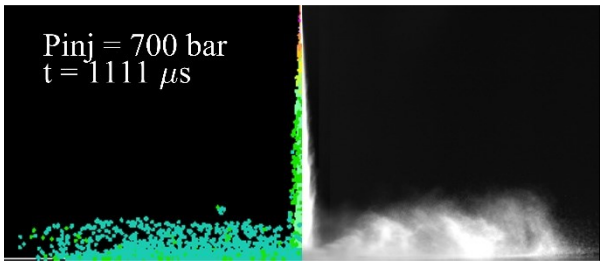

Figure 13: comparison of the experimental and simulated spray plume morphology for an injection pressure of 700 bar at t=1111 μs.

In particular, Figure 12 highlights the slight under-estimation of the simulated thickness.

By analysing Figure 13, the under-estimation of the simulated thickness highlighted in Figure 8(b) is much more pronounced than the one at 500 bar, while the thickness is effectively captured.

Comparing the experimental plume morphologies, it is possible to notice that the contour trace is more defined around the region for which the width is computed. Instead, the contour defining the spray plume thickness is more affected by the actual threshold applied to the images. Consequently, in the case of considering the brighter upper region as the one used to contour the spray plume, the measurement of the experimental thickness can be lower with respect to the data shown in the previous figures. Instead, the region defining the contour for the width calculation appears to be brighter in all the figures, leading to the traces for the experimental width to be kept the same.

Conclusions

The current study is focused on the impact of gasoline spray injected adopting unconventional ultra-high pressure (500 and 700 bar) which are typically implemented during LTC combustions, especially for what concerns the GCI concept. The aim is to providing insights on the behaviour of such fuel during impacting events against the engine walls at low temperature conditions representative of cold start and low load conditions.

The behaviour of the impinged fuel spray plume has been captured by an experimental facility at the CNR-STEMS laboratory. In particular, the axial penetration (thickness) and tangential (width) penetration of the rebound cloud were recorded by means of the Mie-scattering technique. Experiments showed that the spray plume morphology behaves differently depending on the actual injection pressure during the early injection event. In particular, the spray cone angle is greatly affected by the actual injection pressure. In fact, for the injection pressure of 500 bar, the cone angle at the first recorded time (93 μs) is almost 6 degrees. Then, it reduces from 6 to 4 degrees in the following instants. Instead, for the injection pressure of 700 bar, the cone angle is not affected by the injection phase.

Three-dimensional CFD simulations have been conducted to compare the simulated spray plume with the real ones from the experiments. To take into account the transient dynamics highlighted by the experiments, a user-subroutine has been implemented to capture both the cone angle and the liquid length penetration. It has been proven that the tuning of the effective nozzle area during the transient injection phase is a key feature to match the liquid penetration compared to the use of a fixed value for both transient and steady injection phases. In the latter case, under-estimation of 5-10 mm penetration were detected.

Results showed that the plume thickness, width, and overall spray morphology are in good agreement with the experiments. Additional tests will be conducted to analyse the behaviour of gasoline spray impacting on a heated wall to understand other impact regimes as transition and film boiling ones.

References

1. Krishnamoorthi, M., Malayalamurthi, R., He, Z., and Kandasamy, S., “A review on low temperature combustion engines: Performance, combustion and emission characteristics,” *Renew. Sustain. Energy Rev.* 116:109404, 2019, doi:10.1016/j.rser.2019.109404.

2. Sellnau, M.C., Sinnamon, J., Hoyer, K., and Husted, H., “Full-Time Gasoline Direct-Injection Compression Ignition (GDCI) for High Efficiency and Low NOx and PM,” *SAE Int. J. Engines* 5(2):300–314, 2012, doi:10.4271/2012-01-0384.

3. Sellnau, M., Foster, M., Hoyer, K., Moore, W., Sinnamon, J., and Husted, H., “Development of a

Gasoline Direct Injection Compression Ignition (GDCI) Engine," *SAE Int. J. Engines* 7(2):835–851, 2014, doi:10.4271/2014-01-1300.

4. Piazzullo, D., Costa, M., Allocca, L., Montanaro, A., and Rocco, V., "A 3D CFD Simulation of GDI Sprays Accounting for Heat Transfer Effects on Wallfilm Formation," *SAE Int. J. Engines* 10(4):2166–2175, 2017, doi:10.4271/2017-24-0041.

5. Catapano, F., Costa, M., Marseglia, G., Sementa, P., Sorge, U., and Vaglieco, B.M., "An Experimental and Numerical Investigation of GDI Spray Impact over Walls at Different Temperatures," 2016-01–0853, 2016, doi:10.4271/2016-01-0853.

6. Muddapur, A., Sahu, S., Jose, J.V., and T., S., "Spray–wall impingement in a multi-hole GDI injector for split injection at elevated wall temperature and ambient conditions," *Therm. Sci. Eng. Prog.* 33:101367, 2022, doi:10.1016/j.tsep.2022.101367.

7. Zhao, L., Torelli, R., Zhu, X., Naber, J., Lee, S.-Y., Som, S., Scarcelli, R., and Raessi, M., "Evaluation of Diesel Spray-Wall Interaction and Morphology around Impingement Location," 2018-01–0276, 2018, doi:10.4271/2018-01-0276.

8. Seers, P., Reguillet, V., Plamondon, E., Dufresne, L., and Halle´, S., "Evaporation Time of Gasoline and Diesel Fuel Droplets on a Hot Plate: The Influence of Fuel Deposits," *Volume 3: Combustion Science and Engineering*, ASMEDC, Boston, Massachusetts, USA, ISBN 978-0-7918-4864-7: 577–583, 2008, doi:10.1115/IMECE2008-68786.

9. Ravaglioli, V., Ponti, F., Silvagni, G., Moro, D., Stola, F., and De Cesare, M., "Performance Assessment of Gasoline PPC in a Light-Duty CI Engine," 2022-01–0456, 2022, doi:10.4271/2022-01-0456.

10. Stola, F., Ravaglioli, V., Silvagni, G., Ponti, F., and De Cesare, M., "Injection Pattern Investigation for Gasoline Partially Premixed Combustion Analysis," 2019-24–0112, 2019, doi:10.4271/2019-24-0112.

11. Montanaro, A., Allocca, L., Lazzaro, M., and Meccariello, G., "Vapor and Liquid Phases of the ECN Spray G Impacting on a Flat Wall at Engine-Like Conditions," 2016-01–2199, 2016, doi:10.4271/2016-01-2199.

12. Montanaro, A., Allocca, L., and Lazzaro, M., "Iso-Octane Spray from a GDI Multi-Hole Injector under Non- and Flash Boiling Conditions," 2017-01–2319, 2017, doi:10.4271/2017-01-2319.

13. Allocca, L., Montanaro, A., Meccariello, G., Duronio, F., Ranieri, S., and De Vita, A., "Under-Expanded Gaseous Jets Characterization for Application in Direct Injection Engines: Experimental and Numerical Approach," 2020-01–0325, 2020, doi:10.4271/2020-01-0325.

14. Otsu, N., "A Threshold Selection Method from Gray-Level Histograms," *IEEE Trans. Syst. Man Cybern.* 9(1):62–66, 1979, doi:10.1109/TSMC.1979.4310076.

15. Bosch, W., "The Fuel Rate Indicator: A New Measuring Instrument For Display of the Characteristics of Individual Injection," 660749, 1966, doi:10.4271/660749.

16. Lucchini, T., D'Errico, G., Ettorre, D., Brusiani, F., Bianchi, G.M., Montanaro, A., and Allocca, L., "Experimental and Numerical Investigation of High-Pressure Diesel Sprays with Multiple Injections at Engine Conditions," 2010-01–0179, 2010, doi:10.4271/2010-01-0179.

17. Huh, K.Y., Lee, E., and Koo, J., "DIESEL SPRAY ATOMIZATION MODEL CONSIDERING NOZZLE EXIT TURBULENCE CONDITIONS," *At. Sprays* 8(4):453–469, 1998, doi:10.1615/AtomizSpr.v8.i4.60.

18. Payri, R., Gimeno, J., Venegas, O., and Plazas, A.H., "Effect of Partial Needle Lift on the Nozzle Flow in Diesel Fuel Injectors," 2011-01–1827, 2011, doi:10.4271/2011-01-1827.

19. Payri, R., Gimeno, J., Venegas, O., and Plazas-Torres, A.H., "EXPERIMENTAL AND COMPUTATIONAL STUDY OF THE INFLUENCE OF PARTIAL NEEDLE LIFT ON NOZZLE FLOWIN DIESEL FUEL INJECTORS," *At. Sprays* 22(8):687–714, 2012, doi:10.1615/AtomizSpr.2012005810.

20. Pilch, M. and Erdman, C.A., "Use of breakup time data and velocity history data to predict the maximum size of stable fragments for acceleration-induced breakup of a liquid drop," *Int. J. Multiph. Flow* 13(6):741–757, 1987, doi:10.1016/0301-9322(87)90063-2.

21. Bai, C. and Gosman, A.D., "Development of Methodology for Spray Impingement Simulation," 950283, 1995, doi:10.4271/950283.

22. Rosa, G., Villedieu, P., J., D., and Lavergne, G., "A new droplet-wall interaction model," 2008.

23. Stanglmaier, R.H., Roberts, C.E., and Moses, C.A., "Vaporization of Individual Fuel Drops on a Heated Surface: A Study of Fuel-Wall Interactions within Direct-Injected Gasoline (DIG) Engines," 2002-01–0838, 2002, doi:10.4271/2002-01-0838.

24. Spiegler, P., Hopenfeld, J., Silberberg, M., Bumpus, C.F., and Norman, A., "Onset of stable film boiling and the foam limit," *Int. J. Heat Mass Transf.* 6(11):987–989, 1963, doi:10.1016/0017-9310(63)90053-X.

25. O'Rourke, P.J., "Collective Drop Effects in Vaporizing Liquid Sprays," PhD thesis, Princeton University, 1981.

26. Shiller, L. and Naumann, A., "A drag coefficient correlation," 1935, doi:77:318–320.

27. Wakil, M., Uyehara, O., and Myers, P., "A theoretical investigation of the heating-up period of injected fuel droplets vaporizing in air," 1954.

Abbreviations

CFD	Computational Fluid Dynamics
CR	Common-Rail
GCI	Gasoline Compression Ignition
LLP	Liquid Length Penetration